Design progress on the Lynx soft x-ray critical-angle transmission grating spectrometer

Hans Moritz Günther[a] and Ralf K. Heilmann[a,b]

[a]MIT Kavli Institute for Astrophysics and Space Research, Massachusetts Institute of Technology, Cambridge, MA 02139, USA
[b]Space Nanotechnology Laboratory, Massachusetts Institute of Technology, Cambridge, MA 02139, USA

ABSTRACT

Lynx is one of the Surveyor-class mission concept studies for the 2020 Astrophysics Decadal Survey. One of the nominal science instruments for Lynx is a soft X-ray grating spectrometer and our design using critical-angle transmission (CAT) gratings can achieve the required resolving power $R > 5000$ and effective area > 4000 cm^2. We presented an initial optical design in Günther & Heilmann 2019 (JATIS 5, 02), and identified several points where additional ray-trace work can improve our design of the instrument. We add additional non-ideal effects to our ray-traces, namely diffraction and shadowing by the support structures of the gratings membranes and a finite energy resolution of the detector. Taken together, resolving power and effective area do not change much compared to our initial work, but this higher level of detail in the simulations shows that the design is workable in the presence of non-ideal effects.

Keywords: ray-tracing, X-ray optics, critical angle transmission grating, Lynx, Rowland torus

1. INTRODUCTION

Many discoveries in astronomy are only possible with large and expensive missions. Despite the quest to engineer clever instruments, telescopes, and spacecraft with very targeted capabilities, some of the most exciting breakthroughs require an observatory that collects a lot of photons in a short time and feeds them into highly capable, well-calibrated instruments. High-resolution grating spectroscopy is such a science area, where a large collecting area is required to collect enough photons in every wavelength bin. In particular for time-variable sources, there is no alternative to feed the spectrometer with a large mirror.

Since large observatories are expensive to design, build and operate, NASA did select four concepts for detailed studies in advance of the 2020 Decadal Survey. The study of an X-ray telescope is called Lynx.[1] The design reference mission (DRM) for Lynx includes a mirror with a 2 m^2 collecting area at 1 keV and a Point-spread-function (PSF) of 0.5 arcsec half-power-diameter (HPD). The light from this mirror can feed into three different instruments. At the focal point, users can choose from the High-Definition X-ray Imager (HDXI)[2] or a microcalorimeter.[3] Additionally, X-ray gratings can be inserted into the beam to diffract the soft X-rays to a dedicated detector. This setup is called the X-ray grating spectrometer (XGS). Two different grating technologies are feasible, either reflection gratings[4] or diffraction gratings.[5] We have previously (Ref. 5) described design and performance of an XGS design based on critical-angle transmission (CAT) gratings and in this work we describe further progress in studying the CATXGS.

In Section 2 we describe the design of the CATXGS (simply abbreviated "XGS" from now on). In Section 3 we explain how the ray-traces are done, which details were added to the ray-trace code, and how they impact the XGS performance. Section 4 presents an alignment budget. We close with a short summary in Section 5.

Send correspondence to H.M.G. (E-mail: hgunther@mit.edu, Telephone: 1 617 253 8008)

2. THE CATXGS DESIGN

We summarize the setup of our XGS design here to set the scene for the discussion in the following sections. See Ref. 5 for details and supporting figures.

The diffraction elements of the CATXGS are CAT gratings.[6,7] Those gratings are etched from silicon wafers. The grating bars have very high aspect ratio and are designed to be illuminated at a slight angle (called "blaze angle") to the incoming beam. For Lynx, we plan gratings that are 5.7 μm deep with a period of 200 nm. In this layout, the X-rays are incident on the sidewalls of the grating bars close to the critical angle. This design increases the grating efficiency and directs almost all diffracted power to one side. The peak of the diffracted power is located at twice the blaze angle and only a limited number of X-ray detectors is needed to capture most of the diffracted power. The grating bars are held in place by supporting structures running perpendicular to the grating bar direction, which we call L1 supports. The L1 support bars are 500 nm thick and have a period of 5 μm, thus they cover 10% of the geometric open area of the gratings. As additional support, hexagonal L2 support structures sit below the membrane of grating bars and L1 supports. The L2 structure is 0.5 mm deep and has a periodicity around 1 mm. The thickness of the walls is chosen such that the L2 structures have a geometric coverage around 10% (Fig. 1, left).
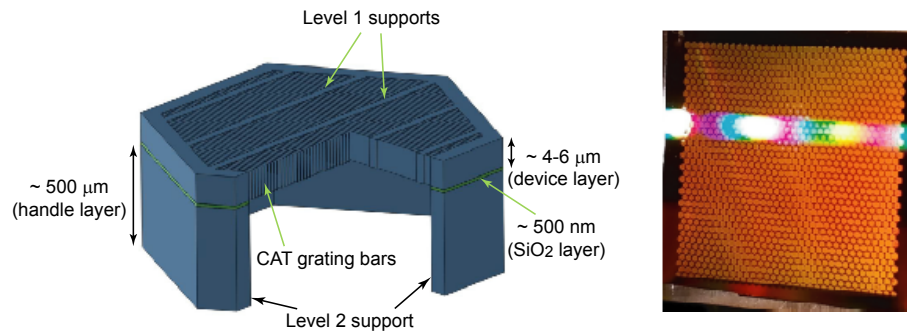

Figure 1. Left: Schematic depiction of the structural hierarchy of the CAT grating membrane (see text). Right: Photograph of a back-illuminated 32×32 mm^2 prototype CAT grating membrane, showing the hexagonal L2 mesh and optical diffraction from the L1 mesh.

For the XGS, in this work we assume individual rectangular grating facets 50 mm on one side and 20 mm on the other, surrounded by a thin Si frame that allows bonding them into holders (Fig. 1, right) which can be mounted to support structures. Using larger gratings reduces the area of the shadows cast by frames and mounting structures, but, since the gratings are flat, causes larger deviations from the mathematical surface that would give us the best spectroscopic focus. Reference 5 discusses these trade-offs in more detail. Grating frames are arranged on a Rowland torus.[8] To reduce the average distance between flat CAT gratings and torus surface, the torus is slightly tilted, i.e. the optical axis of the telescope is not exactly perpendicular to the symmetry axis of the torus,[9,10] see Ref. 5 for details.

In order to achieve the best spectral resolution, the detectors are tangent to the Rowland torus, too. Figure 2 shows a rendering of the proposed layout.

3. RAY-TRACE CALCULATIONS

Our analysis of the Lynx XGS design is based on analytic considerations and geometric ray-traces. In a geometric ray-trace, we follow the path of individual rays through the system using the MARXS code.[11,12] MARXS is written in Python and available under the GNU license v3. We have added the effects discussed in the following sub-sections (diffraction by L1 support bars, diffraction by L2 hexagons, and geometric shadowing by L2 hexagons) to the MARXS codebase and the model will be contained in the upcoming 1.2 release of MARXS. We used MARX version 1.2.dev743 (commit hash: 3d1e5d248b) for the simulations shown here. The code is
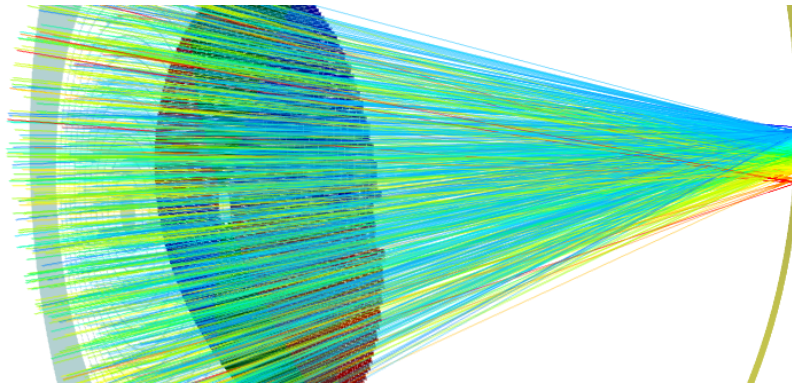
Figure 2. Rendering of the XGS design. Photons enter from the mirror on the left. Gratings are shown in different colors for six different sectors. In the DRM only four out of six sectors will be filled with gratings. The figure shows photon path for photons with 1 keV (about 1.2 nm). Photons are colored according to the diffraction order. The far side of the Rowland torus where the detectors are located is marked in yellow, for the XGS only a limited number of detectors will be used covering about 200 mm.

available on github[*]. Lynx XGS specific code is available at github as well[†]; we used the version with commit hash 19a8a4b.

The optical elements of Lynx are treated with different degrees of detail. For the mirrors, we use the dimensions of the meta-shell optic in the DRM. However, since not all details of this design are yet decided, we use a simplified model that captures the important properties of the mirror. Instead of simulating individual shells, we only treat the mid-plane of the mirror optic. All photons hitting this plane are directed to the focal plane by an ideal lens. We then add two scattering terms, one in the plane of reflection and one out of the plane of reflection, which represent figure errors and mirror roughness. For each photon we draw the angle of the scatter from a Gaussian distribution such that the PSF matches the 0.5 arcsec HPD prescribed in the DRM. MARXS is probability-tracking, which means that each ray has an associated survival probability. In the mirrors, the survival probability of each photon is updated according to the reflectivity of the mirror for the specific incidence angle and photon energy. Since the position of the mirror support spiders is not yet specified in detail, they are not treated as explicit objects in the ray-trace. Instead, the survival probability of each photon is reduced by the geometric coverage fraction of the support spiders. With a more advanced design, we would ensure that, as much as possible, the support structures holding the grating facets are aligned with the mirror support spider. Thus, the current way of "smearing out" the effect of the support spiders on each photon leads actually to a reduced predicted effective area.

A geometric ray-trace cannot predict diffraction, which critically depends on the wave nature of light. Instead, the diffraction efficiency of the CAT gratings must be pre-calculated using other means or measured in the laboratory and diffraction efficiencies are tabulated as a function of photon energy and incident angle. When a ray intersects a grating membrane, MARXS calculates the relevant angles and draws the order that a photon is diffracted into from the tabulated probabilities.

On the detector, each ray is treated as an individual detected photon. In our model, we simulate a cylindrical detector with follows the Rowland torus exactly and a detector consisting of 17 flat pieces which are tangent to the Rowland torus. The latter detector provides simulations with realistic chip gaps, but the earlier avoids pathological cases that can come up when simulating a grid of e.g. different misalignments that cause the signal studied to move into and out of a chip gap.

In the following sub-sections we detail improvements to the ray-trace that we made compared to Ref. 5.

---

[*]https://github.com/chandra-marx/marxs
[†]https://github.com/hamogu/marxs-lynx

3.1 L1 diffraction

The L1 support bars form a diffraction grating perpendicular to the grating bars of the main grating. Since they are etched from the same layer of silicon, they have the same depth. The period of the L1 bars is much larger and thus they diffract to much smaller angles. Importantly, their diffraction efficiency is also much lower because the grating bars cover a smaller fraction of the area and, because they are not blazed, they operate not at the critical angle. In our implementation, we diffract photons first through the grating bars and then independently chose the diffraction order for the L1 support. This is an approximation, since the gratings are co-located, and the second grating is not far away enough to be in the far-field limit for diffracted rays from the first. However, we currently have no reliable theoretical predictions for the combined efficiency of gratings bars and L1 support bars. On the other hand, predictions that treat gratings bars and L1 separately, are qualitatively consistent with the L1 diffraction observed in an X-ray beamline. In the simulation, we use the diffraction efficiencies as predicted for the L1 support structures that are tested in the laboratory now. For Lynx, we will produce gratings that are deeper (5.7 μm vs. 4.0 μm), but have L1 bars only half as thick. Thus, we expect this to be a conservative estimate.
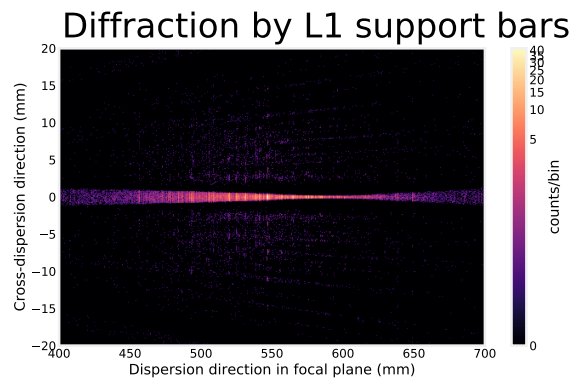

Figure 3. Simulated detector image of an emission line source (the model for the simulation matches the active star EQ Peg A). Note the x and y axis are shown in very different scales. Counts are shown on a logarithmic scale. The bright band of varying thickness in the middle is the main signal, above and below are rays that are dispersed by the L1 support bars. The simulations include neither astrophysical nor instrumental background.

Figure 3 shows a simulation of a point source with a spectrum of a weak continuum with strong emission lines. The model for this particular observation is taken from a Chandra observation of the active star EQ Peg A. In the center of the image is the main signal. This distribution is wider on the left and right on the image and goes through a minimum around 600 mm. The Rowland torus optimizes the spectral resolution, i.e. the width of the signal in dispersion direction, but at the cost of a wider distribution in cross-dispersion direction. In the tilted torus layout we have chosen for the XGS, there are two minima in cross-dispersion direction. The first one is at the position of the zeroth order (not shown here), the second one is located where the Rowland circle intersects the symmetry axis of the torus again.

Above and below the main stripe of signal is a large area with photons that looks almost like a diffuse emission region. This is signal dispersed by the L1 structures. The dispersion angle is given by the diffraction equation that governs any diffractive grating:

$$n\lambda = d\sin(\alpha) \tag{1}$$

where d is the period of the structure, α is the dispersion angle, λ is the wavelength of the photons in question and n the diffraction order. Almost 90% of the signal is found in the $n = 0$ order (the central strip), but a few % go into orders $n_{\mathrm{L1}} = -3$, -2, -1, 1, 2, and 3. For a CAT grating, at any particular position in the dispersion direction, there are photons of different energies (see Fig. 6), at some positions photons of eight to ten different energies fall onto the same detector location. That means that ten different λ values are possible in the equation above, and each of them can be seen in $n_{\mathrm{L1}} = -3$ to 3. Altogether this means that the L1 dispersed orders are not separately visible in the image, but smear together although in some cases, bright emission lines can be seen

individually. For example, around dispersion coordinate 550 mm, there is a single bright emission line, that can be seen individually above and below the main signal, too.

How does L1 cross-dispersion affect the performance of the XGS? Since the L1 bars are made to be exactly perpendicular to the main grating membrane, diffraction on the L1 bars does not impact the resolving power of the instrument. In principle, all the photons dispersed by the L1 bars can still be extracted, provided that the detectors are large enough to capture all L1 orders. However, in practice, we will use only the signal from a limited region in cross-dispersion direction to reduce the background (both astrophysical and instrumental) in the extracted data. The choice of the size of extraction region depends on the details of the observation. For example, a grating observation of a source in the galactic center, where diffuse X-ray emission will cause a large background signal, or an observation taken during a solar flare leading to a large instrumental background, will be best analyzed using a very small extraction region. On the other hand, a bright source in an otherwise X-ray dark field could be extracted from a larger region in cross-dispersion direction to recover the photons dispersed by the L1 bars.

In the most extreme case, all photons dispersed on the L1 bars are lost and the effective area of the XGS is reduced by that factor, which we currently estimate to be $< 10\%$. The effect of the L1 bars can be reduced by reducing the L1 diffraction efficiency. This can be achieved by making the bars as narrow as possible without impacting the mechanical stability of the membrane.

Another approach is to change the spacing of the L1 bars such that it is not uniform but varies pseudo-randomly (with a maximum spacing such that the mechanical stability of the membrane is not compromised). In this case, there will be no coherent diffraction.
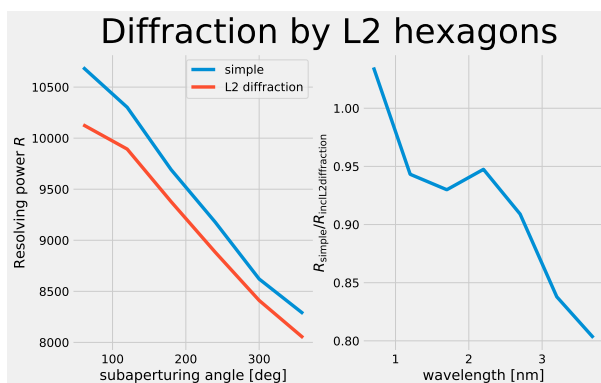
3.2 L2 diffraction

Figure 4. *Left:* Resolving power for a simple simulation ignoring the L2 diffraction and our approximation for the L2 diffraction. Simulations for different sub-aperturing angles are shown. Choosing the best sub-aperturing angle leads to a better R. However, for a higher R the L2 diffraction is more important relative to other effects that broaden the beam. *Right:* Ratio of simulations with and without L2 diffraction for different wavelengths to verify the theoretically expected wavelength dependence.

The L2 support structures are very large compared to the X-ray wavelength (about 1 mm). Thus, diffraction into higher orders is negligible. However, zero-order diffraction can still broaden the beam and thus reduce the spectral resolving power R. For the simulations, we use a very simple prescription. While the L2 support structure is in fact hexagonal we treat it like a circular hole and use the formula for an Airy disk

$$\sin \theta = 1.22 \frac{\lambda}{d} \tag{2}$$

where d is the size of the hole and θ is the angle of the first minimum. We simulate this with the same code we use for scattering. We draw a diffraction angle from a Gaussian distribution that has a width similar to the central Airy disk (we use $\sigma = 0.4\theta$). Figure 4 shows how this reduces the spectral resolving power R of the XGS.

Equation 2 shows that the effect must be larger for longer wavelength and this is reproduced in the simulations. The relative importance of this changes with R. If we design an instrument that achieves high values of R by sub-aperturing and using relatively small grating facets (see Ref. 5 for a discussion) then the L2 diffraction becomes a limiting factor. On the other hand, if we design to the Lynx XGS specification of $R = 5000$ then other effects dominate over the broadening of the L2 diffraction. For the XGS we aim to reduce the geometric coverage by the L2 support structure. The two options for this are to reduce the thickness of the L2 sidewalls or to increase the period of the L2 structures. Looking at Eq. 2 and Fig. 4, it seems promising to increase the size of the L2 period as far as possible without compromising the mechanical stability of the grating membrane since the angle is inversely proportional to d. If d was just twice as large as it is in the current generation of gratings, diffraction by the L2 structure would be only a minor effect for all scenarios we analyze for the XGS. Alternative L2 designs (triangular mesh instead of hexagonal, for example) might provide superior mechanical stability with increased throughput.
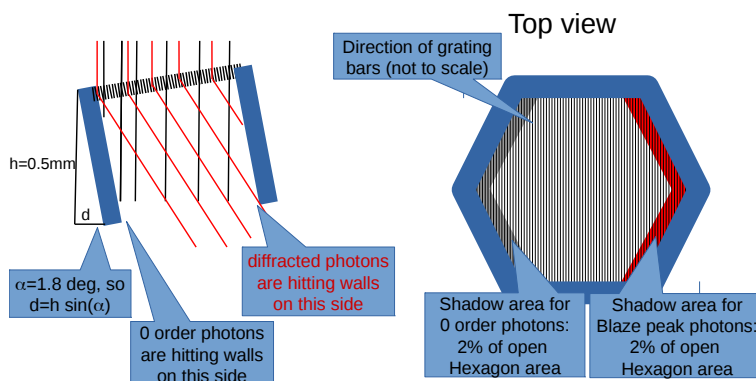
3.3 L2 shadowing

Figure 5. Sketch to illustrate geometric blocking by the L2 sidewalls.

Compared to the grating bars and the L1 support structures, the L2 supports are macroscopic. Presently, the hexagon pattern is $h = 0.5$ mm deep simply because this is a standard silicon wafer thickness. It provides the required stiffness to the grating, but the depth can probably be reduced without compromising survivability. Photons can hit the L2 sidewalls, which will cast a shadow. We expect that all photons that hit the sidewalls are lost. Either they enter the silicon and are absorbed or they are reflected. Because the L2 sidewalls are not polished, such a reflection is very likely to divert the photon away form the area covered by the detector. For a periodic, hexagonal pattern with period p and a width w of the L2 walls (measured in the plane of the grating membrane, see "top view" in Fig. 5), the open fraction is simply

$$f_{\text{open}} = \frac{w^2}{p^2} \ . \tag{3}$$

Depending on the angle α between the incoming ray and the normal to the grating membrane, additional fractional area is blocked (grey or red in the right panel of the sketch in Fig. 5 for the direct light (black) or the diffracted light (red)), respectively:

$$f_{\text{shadow}} = \frac{(p - w)h \sin \alpha}{\frac{\sqrt{3}}{2}p^2} \ . \tag{4}$$

The angle α is the blaze angle (1.6° for the Lynx XGS).

3.4 Energy resolution of the detector

Blazed CAT gratings disperse most light in the direction of the blaze peak, located at twice the blaze angle. This feature is responsible for the high efficiency of CAT gratings and thus a fundamental requirement to reach

the effective area that is the design goal of the Lynx XGS. It also means that a limited number of detectors is sufficient to capture almost all the dispersed light, which makes the XGS efficient in terms of cost and power requirements. On the other hand, this design leads to many spatially overlapping orders, where photons of different wavelengths are detected in the same physical location on the detector. For example, 4.0 nm photons in second order, 2.66 nm photons in third order, 2.0 nm photons in forth order and 1.6 nm photons in fifth order are all detected at the same detector location. Thus, the detector needs to have an intrinsic energy resolution to resolve those orders. The energy difference between two consecutive orders is independent of order number n:

$$\Delta E = E_{n+1} - E_n = \frac{hc}{\lambda_{n+1}} - \frac{hc}{\lambda_n} = \frac{hc}{\frac{d \sin \theta}{n+1}} - \frac{hc}{\frac{d \sin \theta}{n}} = \frac{hc}{d \sin \theta} \tag{5}$$

where h is the Planck constant, c the speed of light, d the period of the grating, and θ the diffraction angle.
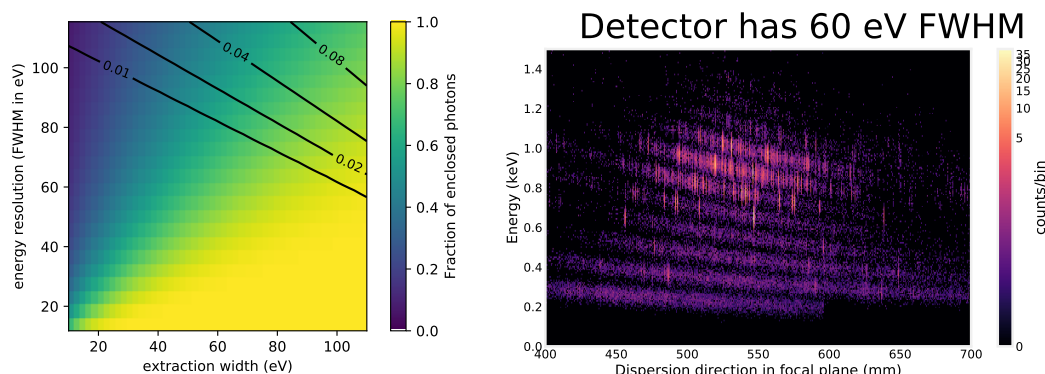

Figure 6. *Left:* The color shows the fraction of photons enclosed in a an order-sorting region given extraction width and detector performance. The contour lines show the fraction of photons from order $n-1$ or $n+1$ that will be detected in order n. *Right:* Simulation of EQ Peg A spectrum shown in Fig. 3, but integrated in cross-dispersion direction. The different orders in this energy-position plot can be discerned by eye. the color scale is logarithmic to highlight faint features. While orders are generally well separated, bright emission lines have enough signal that they can contribute a non-negligible number of photons to neighboring orders.

In practice, all detectors have a finite energy resolution, and thus it is possible that a photon with energy E in diffraction order n is in fact detected with an energy E' which is erroneously associated with order $n+1$. In a typical X-ray analysis procedure today, photons are extracted from a region in energy space that is centered on the expected energy of the diffracted signal. Choosing a narrower region will on the one hand reduce the number of background events and can thus increase the signal-to-noise ratio (SNR), on the other hand, it also means that source photons detected above or below the threshold will be excluded, reducing the detected signal. Assuming that the detector will report a normal distribution for a source of monoenergetic photons, Fig. 6 (left) shows the fraction of photons that is included in the extraction region depending on the width of this region and the performance of the detector. For example, if the extraction width is 80 eV (nominal energy ±40 eV) and the FWHM of the detector energy resolution is also 80 eV, then the detection region contains only about 80% of the diffracted photons. In other words, this reduces the effective area of the XGS by 20%. At the same time, the extraction region for order n will contain about 2% of the photons from order $n-1$ and 2% of the photons from order $n+1$. For many science cases, in particular for emission line sources, contamination from other orders is not a problem as long as all orders are modeled simultaneously using the appropriate response matrix file (RMF) which will contain significant off-diagonal elements. Figure 6 (right) shows an order-sorting plot for an emission line source. However, there are some cases (detection of a weak absorption line on a strong continuum) where the statistical significance of a result can be impacted if the contamination is too strong; detailed simulations are required to quantify this effect.

In summary, the XGS requires detectors with a good energy resolution for order sorting, of order 60 eV FWHM or better.

4. MISALIGNMENT BUDGET

In Ref. 5 we already presented simulations to quantify the impact of misalignment on the performance of the XGS. As a first step, we varied one degree of freedom at a time (e.g. translating the CAT gratings in x direction). One example can be found in Ref. 5, another one in Figure 7, which shows simulations where CAT gratings where rotated around the x-axis (parallel to the optical axis of the telescope), the y-axis (parallel to the dispersion direction) and the z-axis (parallel to the cross-dispersion direction). For each grating, a misalignment angle is
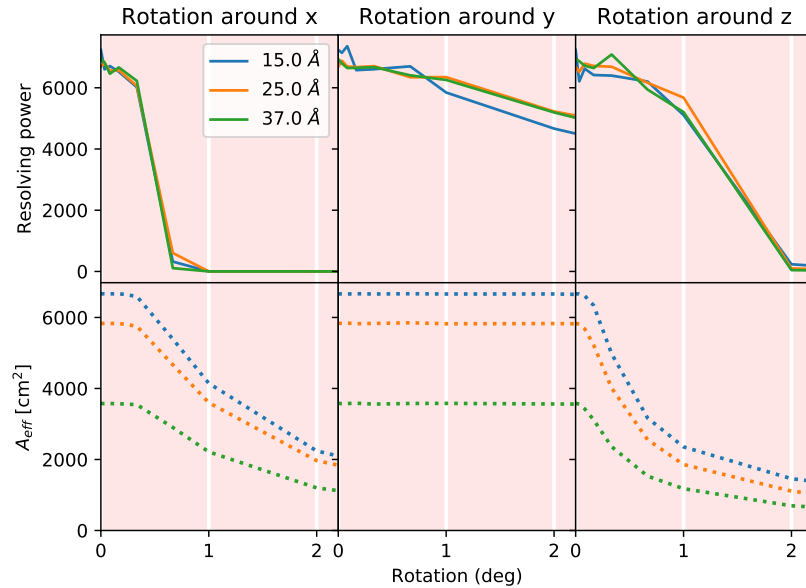

Figure 7. Resolving power and effective area as a function of CAT grating misalignment. Shown here are simulations where all CAT gratings are individually rotated around their centers. The misalignment for each grating is drawn from a normal distribution.

drawn from a normal distribution of a specified width. Once all gratings are misaligned, simulations are run for three different wavelengths. Rotation around the x-axis changes the dispersion direction, such that photons travel a little shorter direction along the nominal dispersion direction and some distance along the nominal cross-dispersion direction before they hit the detector. This widens the spot on the detector in dispersion direction and reduces R. The figure shows that rotation around the x-axis has very little impact on the resolving power as long as the rotation is smaller than about a quarter degree. For larger rotations, this effect begins to dominate over other non-ideal effects and R drops significantly. Rotation around y (the cross-dispersion direction) has very little impact on either resolving power or effective area. Last, rotation around z impacts the effective area first. The XGS is designed for a certain blaze angle. Rotation around z changes the blaze angle, the angle between the incoming photons and the grating membrane normal, and as a result of that photons are diffracted into orders further away from the nominal blaze peak. Since this area is not covered by detectors, the photons are effectively lost, reducing the effective area. It is from plots like this, that we estimate the maximal misalignment that we can tolerate without reducing the performance of the Lynx XGS below the science requirements. Table 1 summarizes our error budget.

It is not computationally feasible to search the entire parameter space varying all degrees of freedom listed in Table 1 at the same time. However, we still need to test how the performance of the XGS for this case as these effects may cancel each other out, add up, add up in quadrature, or depend on each other in some other functional form. We thus take a nominal XGS design and disturb all elements in all directions at the same time, drawing the size of each misalignment from the value in Table 1. We make 100 realizations for this setup and run simulations for three different wavelengths for each of them. The resulting distribution of resolving powers and effective areas is shown in Fig. 9; for comparison the resolving power and effective area of a nominal (without

Table 1. Alignment budget. The numbers given are the 1σ values for a normal distribution. *Numbers in italics mark degrees of freedom that can be adjusted in flight with the camera focussing mechanism.*

alignment	trans x mm	trans y mm	trans z mm	rot x arcsec	rot y arcsec	rot z arcsec
CAT structure to mirrors	1.0	0.50	0.50	36	36	36
individual CAT gratings to structure	0.1	0.25	0.25	360	720	360
Camera to front assembly	*0.1*	1.0	3.0	1800	3600	*36*

misalignments, but including L1 and L2 support structures) XGS is shown in Fig. 8. The distributions of effective areas is fairly peaked and falls on about 97% of the nominal effective area at 25Å, close to the O VII triplet that is important for several of the Lynx science cases. The distribution of resolving powers is broader. At 25Å we can expect at least 85% of the nominal R for 90% confidence. In order to guarantee a higher R or to guarantee 85% of the nominal R with a higher confidence the misalignment budget in Table 1 needs to be tightened. The final numbers for the XGS design will require some trade-off between the optical requirements discussed here and engineering constraints. Some degrees of freedom might be easy to constrain better than given in the table and thus can be tightened, while other might require considerable effort and cost. (For example, the rotational alignment budget for the CAT structure is relatively easy to meet due to the ~ 3 m width of that structure.) We can repeat the simulations with an alignment budget that is tweaked according to those needs. However, the table shows overall very manageable constraints for an XGS with CAT gratings.
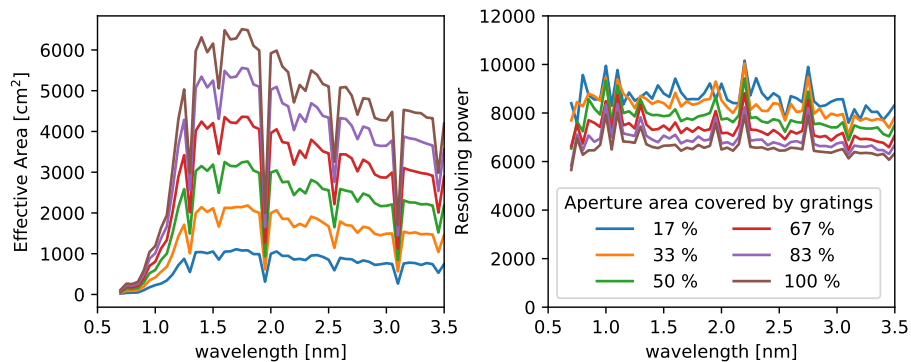

Figure 8. Resolving power and effective area for the nominal (without misalignments) XGS. Drops in effective area (left) happen when one dispersed order falls into a chip gap. Since the resolving power depends on the order, this can show up as a spike in the resolving power (right), if the order in question had a lower than average R.

5. SUMMARY

We have shown a design for the Lynx XGS in Ref. 5 and we summarized its main properties here. Our performance predictions for the XGS are based on geometric ray-tracing and in this work we added several non-ideal effects to the ray-trace that potentially impact the resolving power and the effective area of the XGS. We explain the approximations we chose to treat diffraction by the L1 support bars, diffraction by the L2 hexagonal structure, and geometric shadowing by the L2 sidewalls. We show how these effects impact the XGS performance and give recommendations to reduce the impact. Even at the current design specifications, none of these effects presents a fundamental problem to the XGS design, they merely contribute to the total "error budget" together with geometric aberrations or misalignments.

To study misalignments further, we develop a misalignment budget and simulate the XGS with 100 realizations of this budget. In Ref. 5 we designed the XGS to reach performance numbers about 10% above the science requirements to provide tolerance for alignment and other non-ideal effects. We have now included all outstanding
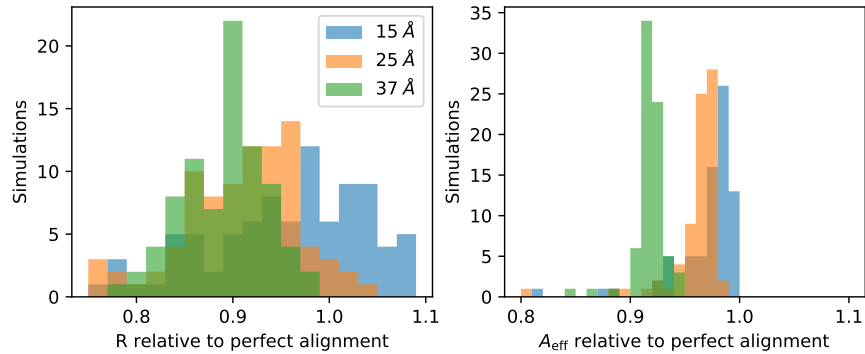
Figure 9. Resolving power and effective area for Lynx XGS simulations with the alignment budget in table 1.

effects identified in Ref. 5 in our simulations and find that the resulting performance of the XGS still matches the science requirements.

REFERENCES

[1] Gaskin, J. A., Swartz, D., Vikhlinin, A. A., Özel, F., Gelmis, K. E. E., Arenberg, J. W., Bandler, S. R., Bautz, M. W., Civitani, M. M., Dominguez, A., Eckart, M. E., Falcone, A. D., Figueroa-Feliciano, E., Freeman, M. D., Günther, H. M., Jr., K. A. H., Heilmann, R. K., Kilaru, K., Kraft, R. P., McCarley, K. S., McEntaffer, R. L., Pareschi, G., Purcell, W. R., Reid, P. B., Schattenburg, M. L., Schwartz, D. A., Sr., E. D. S., Tananbaum, H. D., Tremblay, G. R., Zhang, W. W., and Zuhone, J. A., "Lynx x-ray observatory: an overview," *Journal of Astronomical Telescopes, Instruments, and Systems* **5**(2), 1 – 15 – 15 (2019).

[2] Falcone, A. D., Kraft, R. P., Bautz, M. W., Gaskin, J. A., Mulqueen, J. A., and Swartz, D. A., "Overview of the high-definition x-ray imager instrument on the lynx x-ray surveyor," *Journal of Astronomical Telescopes, Instruments, and Systems* **5**(2), 1 – 6 – 6 (2019).

[3] Bandler, S. R., Chervenak, J. A., Datesman, A. M., Devasia, A. M., DiPirro, M. J., Sakai, K., Smith, S. J., Stevenson, T. R., Yoon, W., Bennett, D. A., Mates, B., Swetz, D. S., Ullom, J. N., Irwin, K. D., Eckart, M. E., Figueroa-Feliciano, E., McCammon, D., Ryu, K. K., Olson, J. R., and Zeiger, B., "Lynx x-ray microcalorimeter," *Journal of Astronomical Telescopes, Instruments, and Systems* **5**(2), 1 – 29 – 29 (2019).

[4] McEntaffer, R. L., "Reflection grating concept for the lynx x-ray grating spectrograph," *Journal of Astronomical Telescopes, Instruments, and Systems* **5**(2), 1 – 8 – 8 (2019).

[5] Günther, H. M. and Heilmann, R. K., "Lynx soft x-ray critical-angle transmission grating spectrometer," *Journal of Astronomical Telescopes, Instruments, and Systems* **5**(2), 1 – 14 – 14 (2019).

[6] Heilmann, R. K., Ahn, M., Bruccoleri, A., Chang, C.-H., Gullikson, E. M., Mukherjee, P., and Schattenburg, M. L., "Diffraction efficiency of 200-nm-period critical-angle transmission gratings in the soft x-ray and extreme ultraviolet wavelength bands," *Appl. Opt.* **50**, 1364–1373 (Apr 2011).

[7] Heilmann, R. K., Bruccoleri, A. R., and Schattenburg, M. L., "High-efficiency blazed transmission gratings for high-resolution soft x-ray spectroscopy," *Proc. SPIE* **9603**, 960314–960314–12 (2015).

[8] Beuermann, K. P., Bräuninger, H., and Trümper, J., "Aberrations of a facet-type transmission grating for cosmic x-ray and xuv spectroscopy," *Appl. Opt.* **17**, 2304–2309 (Aug 1978).

[9] Heilmann, R. K., Davis, J. E., Dewey, D., Bautz, M. W., Foster, R., Bruccoleri, A., Mukherjee, P., Robinson, D., Huenemoerder, D. P., Marshall, H. L., Schattenburg, M. L., Schulz, N. S., Guo, L. J., Kaplan, A. F., and Schweikart, R. B., "Critical-angle transmission grating spectrometer for high-resolution soft x-ray spectroscopy on the international x-ray observatory," *Proc. SPIE* **7732**, 77321J–77321J–11 (2010).

[10] Günther, H. M., Cheimets, P. N., Heilmann, R. K., and Smith, R. K., "Performance of a double tilted-rowland-spectrometer on arcus," *Proc.SPIE* **10397**, 10397 – 10397 – 12 (2017).

[11] Günther, H. M., Frost, J., and Theriault-Shay, A., "MARXS: A Modular Software to Ray-trace X-Ray Instrumentation," *Astronomical Journal* **154**, 243 (Dec 2017).

[12] Günther, H. M., Frost, J., , and Theriault-Shay, A., "Chandra-marx/marxs: v1.1," (Jul 2017).

[13] Astropy Collaboration, Robitaille, T. P., Tollerud, E. J., Greenfield, P., Droettboom, M., Bray, E., Aldcroft, T., Davis, M., Ginsburg, A., Price-Whelan, A. M., Kerzendorf, W. E., Conley, A., Crighton, N., Barbary, K., Muna, D., Ferguson, H., Grollier, F., Parikh, M. M., Nair, P. H., Günther, H. M., Deil, C., Woillez, J., Conseil, S., Kramer, R., Turner, J. E. H., Singer, L., Fox, R., Weaver, B. A., Zabalza, V., Edwards, Z. I., Azalee Bostroem, K., Burke, D. J., Casey, A. R., Crawford, S. M., Dencheva, N., Ely, J., Jenness, T., Labrie, K., Lim, P. L., Pierfederici, F., Pontzen, A., Ptak, A., Refsdal, B., Servillat, M., and Streicher, O., "Astropy: A community Python package for astronomy," *Astronomy and Astrophysics* **558**, A33 (Oct. 2013).

[14] Astropy Collaboration, Price-Whelan, A. M., Sipőcz, B. M., Günther, H. M., Lim, P. L., Crawford, S. M., Conseil, S., Shupe, D. L., Craig, M. W., Dencheva, N., Ginsburg, A., VanderPlas, J. T., Bradley, L. D., Pérez-Suárez, D., de Val-Borro, M., Aldcroft, T. L., Cruz, K. L., Robitaille, T. P., Tollerud, E. J., Ardelean, C., Babej, T., Bach, Y. P., Bachetti, M., Bakanov, A. V., Bamford, S. P., Barentsen, G., Barmby, P., Baumbach, A., Berry, K. L., Biscani, F., Boquien, M., Bostroem, K. A., Bouma, L. G., Brammer, G. B., Bray, E. M., Breytenbach, H., Buddelmeijer, H., Burke, D. J., Calderone, G., Cano Rodríguez, J. L., Cara, M., Cardoso, J. V. M., Cheedella, S., Copin, Y., Corrales, L., Crichton, D., D'Avella, D., Deil, C., Depagne, É., Dietrich, J. P., Donath, A., Droettboom, M., Earl, N., Erben, T., Fabbro, S., Ferreira, L. A., Finethy, T., Fox, R. T., Garrison, L. H., Gibbons, S. L. J., Goldstein, D. A., Gommers, R., Greco, J. P., Greenfield, P., Groener, A. M., Grollier, F., Hagen, A., Hirst, P., Homeier, D., Horton, A. J., Hosseinzadeh, G., Hu, L., Hunkeler, J. S., Ivezić, Ž., Jain, A., Jenness, T., Kanarek, G., Kendrew, S., Kern, N. S., Kerzendorf, W. E., Khvalko, A., King, J., Kirkby, D., Kulkarni, A. M., Kumar, A., Lee, A., Lenz, D., Littlefair, S. P., Ma, Z., Macleod, D. M., Mastropietro, M., McCully, C., Montagnac, S., Morris, B. M., Mueller, M., Mumford, S. J., Muna, D., Murphy, N. A., Nelson, S., Nguyen, G. H., Ninan, J. P., Nöthe, M., Ogaz, S., Oh, S., Parejko, J. K., Parley, N., Pascual, S., Patil, R., Patil, A. A., Plunkett, A. L., Prochaska, J. X., Rastogi, T., Reddy Janga, V., Sabater, J., Sakurikar, P., Seifert, M., Sherbert, L. E., Sherwood-Taylor, H., Shih, A. Y., Sick, J., Silbiger, M. T., Singanamalla, S., Singer, L. P., Sladen, P. H., Sooley, K. A., Sornarajah, S., Streicher, O., Teuben, P., Thomas, S. W., Tremblay, G. R., Turner, J. E. H., Terrón, V., van Kerkwijk, M. H., de la Vega, A., Watkins, L. L., Weaver, B. A., Whitmore, J. B., Woillez, J., Zabalza, V., and Astropy Contributors, "The Astropy Project: Building an Open-science Project and Status of the v2.0 Core Package," *Astronomical Journal* **156**, 123 (Sept. 2018).

[15] van der Walt, S., Colbert, S. C., and Varoquaux, G., "The numpy array: A structure for efficient numerical computation," *Computing in Science & Engineering* **13**(2), 22–30 (2011).

[16] Pérez, F. and Granger, B. E., "IPython: a system for interactive scientific computing," *Computing in Science and Engineering* **9**, 21–29 (May 2007).

[17] Ramachandran, P. and Varoquaux, G., "Mayavi: 3D Visualization of Scientific Data," *Computing in Science & Engineering* **13**(2), 40–51 (2011).

[18] Hunter, J. D., "Matplotlib: A 2d graphics environment," *Computing In Science & Engineering* **9**(3), 90–95 (2007).